International Journal of Greenhouse Gas Control 44 (2016) 74–87

Contents lists available at ScienceDirect

International Journal of Greenhouse Gas Control

journal homepage: www.elsevier.com/locate/ijggc

An integrated site characterization-to-optimization study for commercial-scale carbon dioxide storage

Shuiquan Li[a,*], Morteza Akbarabadi[b], Ye Zhang[c], Mohammad Piri[b]

[a] Enhanced Oil Recovery Institute, University of Wyoming, 1000 East University Avenue, Laramie, WY 82071, USA
[b] Department of Chemical and Petroleum Engineering, University of Wyoming, 1000 East University Avenue, Laramie, WY 82071, USA
[c] Geology and Geophysics Department, University of Wyoming, 1000 East University Avenue, Laramie, WY 82071, USA

ARTICLE INFO

Article history:
Received 23 January 2015
Received in revised form 2 October 2015
Accepted 11 October 2015

Keywords:
Carbon dioxide sequestration
Chase brine injection
Residual trapping
Relative permeability
Moxa arch

ABSTRACT

Injection of supercritical carbon dioxide ($scCO_2$) into deep saline aquifers is considered a promising option to mitigate global climate change. At a storage site, the main objectives of carbon dioxide sequestration are to maximize the volume of $scCO_2$ injected and minimize the leakage risk, while effectively managing formation fluid pressure buildup and the brine displaced by $scCO_2$. An integrated characterization-to-optimization study is carried out for potential commercial-scale deep saline aquifer carbon dioxide storage proposed in western Wyoming. A three-dimensional heterogeneous reservoir model is built for which petrophysical and fluid flow parameters are populated using field characterization data and state-of-the-art laboratory measurements. The measured $scCO_2$ relative permeability end point is low compared to previous measurements on similar sandstones, which poses a challenge for CO_2 flow, formation pressure control, and storage efficiency. By carefully selecting a set of optimal well locations, perforation intervals, and bottomhole pressure constraints that lead to maximum CO_2-in-place and minimal CO_2 breakthrough at the producers, an injection rate ranging from 10.8 to 15.1 Mt/year is achieved for a duration of 50 years. After $scCO_2$ injection ceases, up to 62% of the total injected $scCO_2$ can be immobilized as residual $scCO_2$ in 1000 years. Because of the low $scCO_2$ relative permeability end point, post-$scCO_2$-injection chase brine operation is not found to be an effective means of enhancing residual trapping. Instead, by modulating reservoir fluid pressure, boundary conditions of the reservoir exert a more significant impact on flow. Given the same well configuration and bottomhole pressure constraints, an open reservoir with lateral background flow allows 40% additional $scCO_2$ injection compared to a compartmentalized system without background flow. However, background flow leads to a lower trapping efficiency – after 1000 years post-$scCO_2$-injection, only 54% of the total injected $scCO_2$ is immobilized as residual $scCO_2$. This research suggests that a careful engineering design can contribute to significant CO_2 storage at commercial scales while enhancing storage security. Site-specific multi-phase flow data should be measured for such a design, since for the study site, chase-brine operation is not effective when $scCO_2$ relative permeability is low.

Published by Elsevier Ltd.

1. Introduction

Injection of supercritical carbon dioxide ($scCO_2$) into deep saline aquifers is considered a promising option to mitigate global climate change (IPCC, 2005). In a deep saline aquifer, driven by pressure gradient due to injection, $scCO_2$ will move through aquifer pore space, displacing brine. As $scCO_2$ continues to migrate, brine will begin to replace it, leaving some $scCO_2$ trapped by capillary forces (residual trapping). $scCO_2$ will also dissolve into the brine (dissolution trapping). Mineral trapping occurs from the reactions of dissolved CO_2 with solid grains. Geologic storage of carbon dioxide has been proposed for the state of Wyoming. From 2000 to 2011, energy-related CO_2 emissions in Wyoming increased from 62.9 to 63.8 million tons (Mt) (Stauffer et al., 2009; U.S. Energy Information Administration, 2014) and is further projected to increase with new energy demand, e.g., the proposed Southern California Edison (CEPL) project (Deng et al., 2012; WIA, 2013). Power plants such as these are the chief targets for conversion, to allow for the capture of CO_2 and subsequent sequestration underground.

To store CO_2 at the commercial scale, deep saline aquifers with large storage capacity are required. According to a review of existing storage operations in such environments, strategies that

* Corresponding author.
E-mail address: sli2@uwyo.edu (S. Li).

http://dx.doi.org/10.1016/j.ijggc.2015.10.003
1750-5836/Published by Elsevier Ltd.

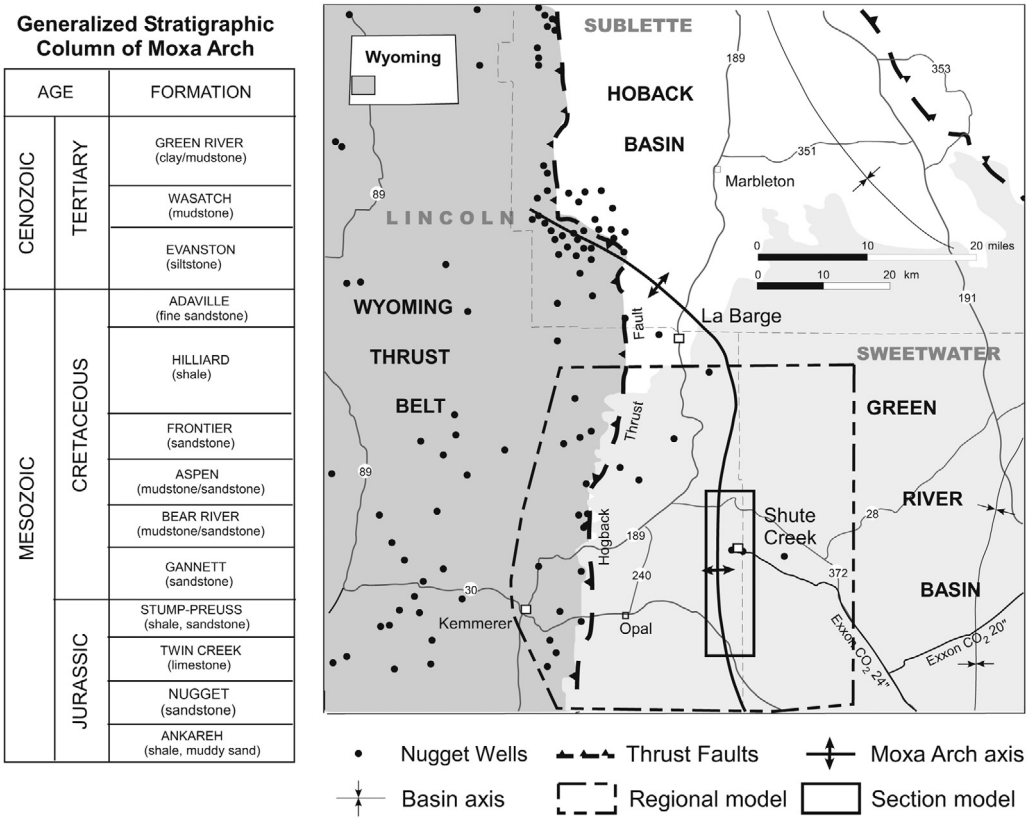

Fig. 1. Study area (Moxa arch) in western Wyoming. A generalized stratigraphic column is shown on the left. A regional model is indicated by the dashed outline within which a section model, centered at the Shute Creek gas plant, is extracted for the simulation study. Regionally, wells that penetrate to the depth of the Nugget Sandstone and deeper are shown.

Table 1
Dimensions and petrophysical properties of the Nugget Sandstone "core" used in this study. $K_{abs,brine}$ is the absolute permeability of the sandstone to brine.

Sample	Length (cm)	Diameter (cm)	Avg. porosity (%) (X-ray)	$K_{abs,brine}$ (mD)	Pore volume (cm^3)
Nugget Sandstone	14.8	3.81	14.28	312	24.09

Table 2
Physical properties of the fluid phases used in this study at 55 °C and 11.0 MPa (Span and Wagner, 1995; Bachu and Bennion, 2009; Batzle and Wang, 1992). IFT is interfacial tension.

Fluids	Density ρ (kg/m^3)	Viscosity μ (mPa s (cP))	$scCO_2$/Brine IFT (mN/m)
$scCO_2$	0.393	0.044	38.15
Brine	1.123	0.91	–

consider multiple injection wells and the optimization of aquifer pore volume sweep efficiency are key to the development of successful commercial-scale storage (Michael et al., 2010). Moreover, previous simulation studies suggest that subsurface boundary conditions – whether the deep saline aquifer has active or stagnant hydrodynamic flow – can significantly impact storage by contributing to active imbibition and dissolution (Li et al., 2011; Liu et al., 2011). Finally, safety and effectiveness of geostorage require that not only the volume of $scCO_2$ injected be maximized, but also that leakage risk be minimized.

The option of using a deep saline aquifer for commercial-scale carbon dioxide storage has pros and cons. Saline aquifers often have large storage volumes and are easily accessible to CO_2 point sources. However, it can be difficult to locate perfectly sealing caprocks at the extent of the plume footprint created by commercial-scale storage. At such scales, a variety of potential leakage pathways can exist inside and above the storage formation, including faults/fractures, lateral facies changes in the caprocks, and possibly leaky abandoned wellbores (Fitts and Peters, 2013; Song and Zhang, 2013; Shukla et al., 2010; Rosenbauer et al., 2005). To reduce migration and the subsequent encounters of leakage pathways, $scCO_2$ needs to be immobilized in the storage formation at or near the injection site. In addition, during injection, fluid pressure buildup can create additional leakage pathways if formation and caprocks experience geomechanical failures (Garridoa et al., 2013; Vilarrasa et al., 2014; Olabode and Radonjic, 2013; Smith et al., 2011; Mbia et al., 2014; Martinez et al., 2013). Finally, deep aquifer brine can be displaced into overlying formations via distinct pathways or diffusion, posing contamination hazards for shallow drinking water aquifers. Heavy metals and toxic compounds, for example, can be mobilized and transported to the near-surface environment by the displaced brine (Kharaka et al., 2009). All these factors must be taken into consideration when designing and executing a commercial-scale geostorage project in a deep saline aquifer.

To address the above issues, various strategies have been proposed that aim to achieve commercial-scale storage with enhanced storage security (a large fraction of the $scCO_2$ is immobilized at or near the injection site), while limiting migration and leakage (Flett et al., 2008; Qi et al., 2009; Surdam et al., 2009). These strategies may include: (1) using brine producers during $scCO_2$ injection to control formation fluid pressure buildup (Li et al., 2011), (2)

injecting chase brine after $scCO_2$ injection to enhance residual trapping and dissolution (Juanes et al., 2006; Qi et al., 2009), and (3) limiting brine migration from the injection site via recycling, where brine is used for both pressure management and chase brine operations. As proposed by Qi et al. (2009), the use of chase brine can lead to active imbibition, immobilizing $scCO_2$ at the injection site in both dissolved and residually trapped forms, while minimizing mobile $scCO_2$. As a result, $scCO_2$ migration can be limited, reducing the need for a perfectly sealing caprock at large scales.

The proposed strategies are tested in a feasibility study of commercial-scale carbon dioxide storage in the Jurassic-aged Nugget Sandstone of the Moxa arch region in western Wyoming (Fig. 1). The proposed injection site is at Exxon's Shute Creek Gas Plant where infrastructure including injection wells and CO_2 pipelines already exists. Here, the Nugget Sandstone is a deep (approximately 17,060 ft (5200 m) below land surface) and regionally extensive saline aquifer with an average thickness of approximately 800 ft (240 m), which underlies and is adjacent to several coal-fired power plants, including the 2.1 Giga Watt (GW) Jim Bridger power plant. The Moxa arch anticline hosts natural gas in the Frontier Sandstone, which overlies the Nugget Sandstone, attesting to the sealing capacity of low-permeability caprocks above the storage formation (Harstad et al., 1996). At the Shute Creek gas plant, acid gas disposal into the Madison Limestone has been ongoing since 2005, at a rate of 60 MMscf/day, without reporting leakage (Huang et al., 2011). The Madison Limestone is a deep saline aquifer lying at an even greater depth than the Nugget Sandstone. Furthermore, in the surrounding area, few wells have been perforated in these deeply buried formations, reducing leakage risk via wellbores (Fig. 1). With the existing infrastructure, the Nugget Sandstone underlying the gas plant is considered a prime candidate formation for CO_2 storage.

For the Shute Creek gas plant storage site, this research carries out an integrated characterization-to-optimization study for the Nugget Sandstone saline aquifer. A variety of field characterization data have been collected and analyzed for this formation to understand its subsurface structure as well as its porosity and permeability distribution (Li et al., 2011). Laboratory experiments have been conducted on Nugget Sandstone outcrop samples to measure $scCO_2$/brine relative permeabilities under high fluid temperature and pressure conditions. A subsurface reservoir model of the sandstone formation, centered at Shute Creek, was built previously using geostatistical techniques (Li et al., 2011). It is upscaled in this study to create a coarse flow simulation model with which streamline simulation is conducted to identify reservoir connectivity and thus optimal locations for placing $scCO_2$ injection and brine production wells. With the optimal well design, compositional simulation is conducted to model $scCO_2$ injection for 50 years, followed by chase brine operation (30 years) and a monitoring period (1000 years). Because CO_2 fluid-rock reactions are generally found to be limited in quartz-rich sandstones and the Nugget Sandstone is an eolian sandstone with relatively simple mineralogy (Cox et al., 1994), mineral reactions and the associated mineral storage are not considered in the simulations (Bennion and Bachu, 2005; Audigane et al., 2007; Kampman et al., 2014). In this study, by integrating field data, numerical modeling, and laboratory measurements, well design and carbon dioxide storage have been optimized for a particular reservoir. During CO_2 injection, by optimizing well locations, a rate ranging from 10.8 to 15.1 Mt/year is achieved with the laboratory measured $scCO_2$/brine relative permeabilities. This rate corresponds to annual CO_2 production rate from a medium-sized Wyoming power plant, thus commercial-scale storage can be achieved at the study site.

In the following sections, experimental measurements, field characterization data, and modeling methods are described, followed by results that illustrate how CO_2 injection and long-term storage can be optimized for commercial-scale carbon sequestration at the study site.

2. Method

Laboratory experiments conducted to measure the $scCO_2$/brine relative permeability of the Nugget Sandstone are described, followed by a description of the field characterization data and how they are integrated using geostatistical techniques to create a heterogeneous subsurface reservoir model for the proposed deep saline aquifer storage site. This model is first analyzed for permeability connectivity, which facilitates the selection of optional well locations. Then CO_2 simulations are carried out to maximize commercial-scale storage, where both the injection rate and the amount of residual trapping are optimized.

2.1. Core-flooding experiments

To characterize the fluid flow properties of the Nugget Sandstone in the laboratory, we present information about the rock sample, experimental conditions, setup, and procedure used in this study. Results obtained from these experiments were then employed in the reservoir simulation of $scCO_2$ storage.

2.1.1. Rock sample, fluids, and experimental conditions

A series of unsteady-state core-flooding experiments was performed on a consolidated, naturally-occurring Nugget Sandstone "core" sample obtained by drilling into an outcrop rock specimen. Due to industry restriction to sampling wells in the study area, the outcrop specimen was acquired in the Red Canyon on the southern end of the Wind Rivers in Wyoming, which is located approximately 86 miles northeast of Shute Creek. The location of this specimen is LAT – 42° 36′47.09378″, and LON – 108° 36′15.13693″. At this location, Nugget Sandstone forms an outcrop on the northern margin of the Greater Green River Basin, although the formation is deeply buried at the Shute Creek Gas Plant within the basin. Thus, the outcrop sample is considered an analog for the reservoir rock at depth, whereas during the laboratory experiment it is subject to formation conditions.

Porosity of the sample was measured using an X-ray imaging technique. Absolute brine permeability was measured using a standard core-flooding setup. Dimensions and petrophysical properties of the Nugget Sandstone "core" are listed in Table 1. The measured porosity and permeability are consistent with those obtained from wireline logs and previous core measurements of the Nugget Sandstone (Li et al., 2011).

In the core-flooding experiments, a highly pure $scCO_2$ and brine with a 10 wt% sodium iodide (NaI), 5 wt% sodium chloride (NaCl), and 0.5 wt% calcium chloride ($CaCl_2$) composition were used as the fluids. The temperature and pressure of the experiments were 55 °C and 11 MPa, respectively. Under these conditions, CO_2 remained in the supercritical phase (Span and Wagner, 1995) throughout the experiment. These conditions reflect subsurface conditions, although of a shallower depth than the proposed formation (Audigane et al., 2007; Kampman et al., 2014; Span and Wagner, 1995). At this stage, higher temperature and pressure conditions were avoided due to safety issues associated with the $scCO_2$ experiments. Because of the relatively high Nugget Sandstone porosity and absolute permeability, as observed in well log data and from core measurements, the effect of greater depth on the relative permeability is considered limited. In Table 2, physical properties of the fluid phases at the experimental conditions are listed.

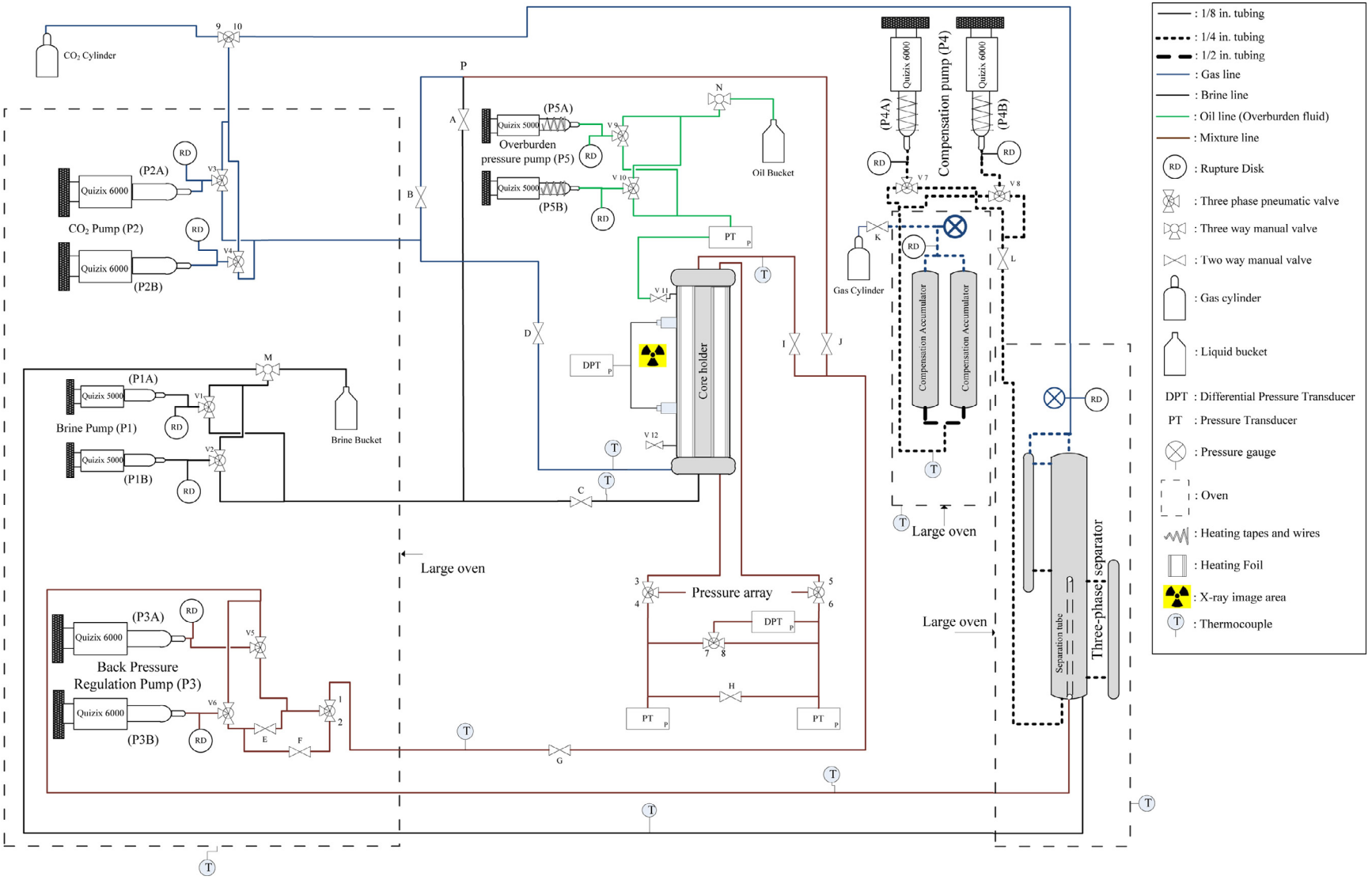

Fig. 2. Schematic flow diagram of the experimental setup used in this work (Piri, 2012).

2.1.2. Experimental setup and procedures

In the unsteady-state core-flooding experiments, to measure $scCO_2$/brine relative permeabilities, four drainage-imbibition experiments were performed for which a multi-phase flow reservoir-condition core-flooding setup was used (Fig. 2; Piri, 2012). The facility consists of a medical CT scanner (Universal HD-350E-V), five dual-cylinder Quizix pumps, a 3500 cm^3 three-phase separator, Rosemount pressure transducers, Hassler-type aluminum core holder, Hastelloy accumulators, as well as several thermocouples at different locations along the flow paths. To maintain a uniform temperature throughout the system, three mechanical convection ovens were used, which contain pumps, separator, and accumulators. The majority of the wetted parts of the facility are made of Hastelloy to prevent corrosion. During the experiment, in order to prevent the diffusion of $scCO_2$ into the sleeve and the overburden fluid, the core sample and the sleeve were wrapped with several layers of Teflon tape and aluminum foil.

During the preparation process, the setup was cleaned thoroughly and vacuumed for several hours to remove air. Pump 4 (P4) and 3 (P3) were used to inject appropriate amounts of brine and $scCO_2$, respectively, into the separator and accumulators. After saturating the core sample with the fluid phases, P3 was employed to inject additional $scCO_2$ to increase the fluid pressure while the heaters and ovens were turned on to increase the temperature, which also helped to pressurize the system. After establishing the pre-specified pressure and temperature of 11.0 MPa and 55 °C, the fluids were re-circulated – by-passing the core holder – for several days to generate thermodynamic equilibrium between the two phases under the experimental conditions. Meanwhile, the core was placed into the core holder and was flushed with $scCO_2$ to eliminate any trapped air, and then the core was vacuumed. At the end of this process, brine-saturated $scCO_2$ was injected into the core to fully saturate the sample. The core was then scanned by the CT scanner to acquire a reference scan (CT_{gc}). This was followed by the injection of the $scCO_2$-saturated brine to fully saturate the sample and to establish $S_w = 1$, after which the core was imaged again to generate another reference scan (CT_{wc}). The effluent mixture from the core was retracted by a Quizix pump (P4) at constant pressure to establish a stable boundary condition, which was necessary for this experiment as the fluids are highly miscible. Note that the CT numbers represent the quantitative characterization of the materials' ability to pass the X-ray. These numbers contain the contribution of each fluid phase in the pore space (Sahni et al., 1998). More detailed information about the experimental setup and procedure is provided elsewhere (Akbarabadi and Piri, 2013).

To measure the relative permeabilities, the first drainage experiment was started by injecting brine-saturated $scCO_2$ at a low flow rate and gradually increasing this rate to a pre-specified maximum flow rate ($Q_{CO_2}^{max}$). After achieving a stable condition at which the differences between two consecutive measurements of the saturation and pressure profiles across the core were less than 1%, the core was imaged to find the initial brine saturation (S_{wi}). At this point, to initiate the imbibition flow test, the core was subjected to $scCO_2$-saturated brine injection at a very low flow rate. The imbibition experiment was considered complete when $scCO_2$ saturation did not change with a slight increase in the brine flow rate. The core sample was then scanned and a residual $scCO_2$ saturation (S_{CO_2r}) was calculated. Prior to the drainage test, the core was re-saturated with brine through an extensive period of brine injection to establish $S_w = 1$. This process took up to 3 days. During this process, brine flow rate was varied from 0.4 to 14 cm^3/min. At the end of each step, pressure difference along the core and saturation distribution were recorded, and a new drainage-imbibition cycle was initiated with a higher $Q_{CO_2}^{max}$. The maximum $scCO_2$ flow rates used in the core-flooding experiments were 2.5, 5, 10, and 20 cm^3/min, which resulted in different S_{wi}. At the end of each drainage and imbibition cycle, pressure differences across the core were recorded and the average saturations measured. The pressure data were then used to calculate brine and $scCO_2$ relative permeabilities.

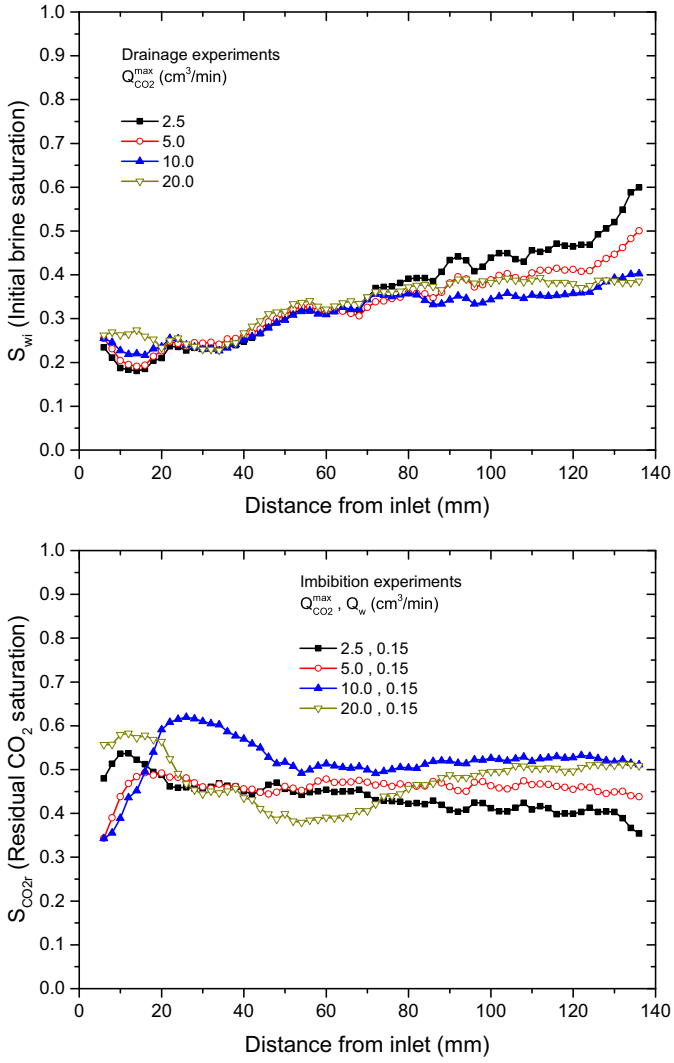

Fig. 3. Variation of (top) initial brine saturation and (bottom) residual CO_2 saturation along the length of the Nugget Sandstone.

2.1.3. In situ saturation measurements

The in situ saturations at the end of each experiment and also when the core was fully saturated with each fluid phase were measured using the images obtained from the scanner with a resolution of 250 μm per slice and an energy level of 130 kV and 100 mA. The saturations were determined by the following equations:

$$S_w = \frac{CT_c - CT_{gc}}{CT_{wc} - CT_{gc}} \quad (1)$$

$$S_g = 1 - S_w \quad (2)$$

where CT_c is acquired from the CT images of the core containing two fluid phases during the experiment. CT_{wc} and CT_{gc} are obtained when the core is fully saturated with brine and $scCO_2$ at the temperature and pressure conditions of the experiment, respectively. This method enables us to calculate the saturation profile along the length of the sample. Fig. 3 provides the variation of brine

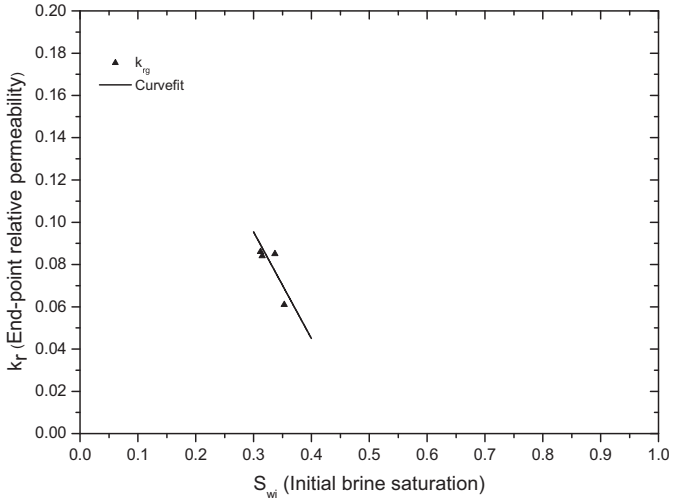

Fig. 4. Unsteady-state end-point $scCO_2$ drainage relative permeabilities for Nugget Sandstone.

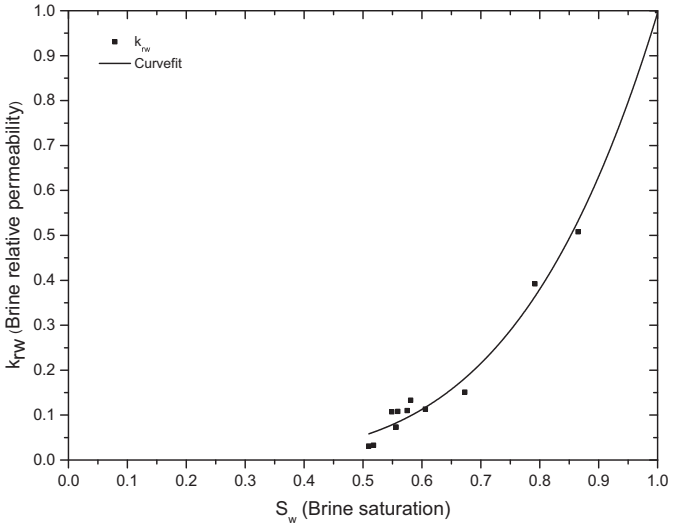

Fig. 5. Unsteady-state brine relative permeabilities during imbibition and dissolution experiments for Nugget Sandstone.

Table 3
Pressure difference values obtained at the end of drainage and imbibition experiments.

Drainage				Imbibition			
Q_{CO_2} (cm^3/min)	S_{wi}	ΔP (kPa)	k_{rg}	Q_w (cm^3/min)	S_w	ΔP (kPa)	k_{rw}
2.5	0.352	14.48	0.061	0.15	0.581	8.27	0.133
5.0	0.337	20.82	0.085	0.15	0.556	15.17	0.073
10.0	0.315	42.20	0.084	0.15	0.518	33.10	0.033
20.0	0.312	82.74	0.086	0.15	0.490	35.85	0.031

saturation along the length of the sample at the end of each drainage and imbibition step.

2.1.4. Relative permeability

With the measured pressure difference along the core and the measured in situ saturations at the end of each drainage-imbibition cycle, relative permeability of each fluid phase is calculated using the multi-phase version of Darcy's Law:

$$k_{ri} = \frac{Q_i \times \mu_i \times L}{K_{abs} \times A \times \Delta P_i} \quad (3)$$

where Q_i, μ_i, L, K_{abs}, A, and ΔP_i are the flow rate and viscosity of fluid phase i, length of the core sample, absolute permeability, cross-sectional area, and pressure difference across the core, respectively.

Fig. 4 illustrates the unsteady-state $scCO_2$ relative permeability at the end of each drainage process. The maximum measured $scCO_2$ relative permeability is less than 0.1. $scCO_2$ end point relative permeability, reported from the literature, is typically greater than 0.1 (Bennion and Bachu, 2005, 2006). Bennion and Bachu (2005) reported maximum $scCO_2$ relative permeability of 0.11 for the Ellerslie Sandstone, which is consistent with the Nugget Sandstone measurement. However, the low $scCO_2$ relative permeability poses a challenge for CO_2 flow, formation pressure control, and ultimately, storage efficiency in the Nugget Sandstone. Please note that using the integral version of Darcy's law might lead to underestimating the non-wetting phase relative permeabilities (Pini and Benson, 2013; Levine et al., 2014). Also, the pressure drops used to calculate relative permeabilities were measured across the core sample, which might include the capillary end effects. This may also introduce inaccuracy in the final results. However, by employing high CO_2 flow rates during the drainage processes, the impact of end effects on relative permeabilities was minimized. Moreover, in recent studies (Akbarabadi and Piri, 2013, 2015), it was reported

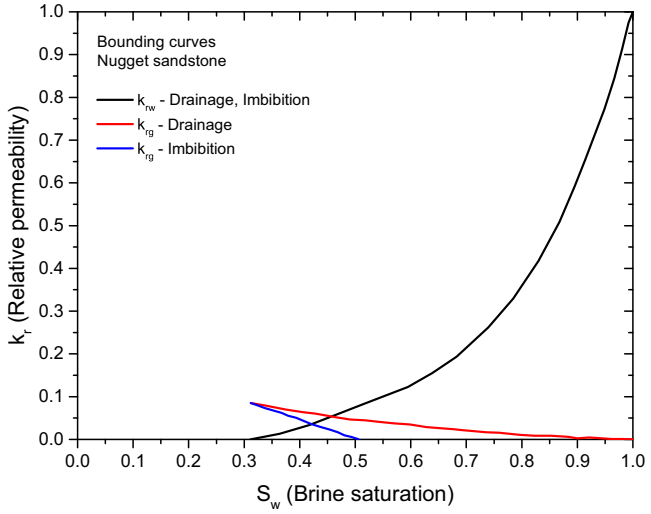

Fig. 6. Drainage CO_2/brine relative permeability bounding curves.

that during the $scCO_2$ flooding, the wettability of the rock surfaces was changed towards the less water-wet condition, which also might lead to lower end-point $scCO_2$ relative permeabilities (Levine et al., 2014). Fig. 5 illustrates the results of the brine relative permeability at the end of each imbibition experiment as well as during the dissolution process. Table 3 lists the values of the pressure differences corresponding to each flow rate used in this study.

Fig. 6 illustrates a set of relative permeability models that are created by fitting known functions to the experimental data. For example, only two relative permeability end points were measured for the bounding $scCO_2$ imbibition curve. Thus based on a known model, which was successfully fitted to the experimental data for the Viking Sandstone (Bennion and Bachu, 2008), a similar function is fitted to the bounding imbibition end point relative permeabilities of the Nugget Sandstone.

2.2. Reservoir modeling

The Nugget Sandstone is an eolian deposit with a lithology dominated by sandstone with minor amounts of siltstone and mudstone. It contains cross-bedded to low-angle, or horizontally bedded, fine

to coarse sands deposited in dune and inter-dune environments (Lindquist, 1983). It contains a lower thinly-bedded facies and an upper more thickly stratified facies, where the lower facies, which on average corresponds to approximately 1/3 of the formation thickness, and has a greater permeability variability; while the upper facies is relatively more homogeneous (Picard, 1975; Li et al., 2011). Paleocurrent studies suggest that the main Nugget deposition occurred along N20E to N70E (Doelger, 1987), which is adopted for the direction of the correlation axes in facies and petrophysical modeling. From interpreting seismic data north of Shute Creek as well as wireline logs in the surrounding region, several porous intervals with low clay volumes have been identified to possess sufficient pore volume to accommodate $scCO_2$ storage (Li et al., 2011). To estimate CO_2 storage at the Shute Creek injection site, a reservoir model of the Nugget Sandstone was built integrating all the available subsurface data. In the following subsections, an overview of the model building process is provided, while detailed information about the site characterization data and their interpretation can be found in Li et al. (2011).

2.2.1. Field characterization data

To build the reservoir model, public-domain subsurface characterization data have been assembled, digitized, and screened for accuracy at the regional scale (Harstad et al., 1996). Data include wireline logs from 165 wells perforating the Nugget Sandstone, which were obtained from Wyoming Oil & Gas Conservation Commission (WOGCC), 785 feet (239 m) of Nugget core porosity and permeability measurements (WOGCC), four geological cross sections (Lamerson, 1982; Royse, 1982), and one regional isopach map (Peterson, 1972; MacLachlan, 1972). Here, it should be pointed out that portion of the 165 wells are out of the regional model, and their log data are borrowed to build the experimental variogram models as the analogue ones of the study site. The well logs include spontaneous potential, resistivity, density, gamma ray, sonic, neutron logs, and a limited number of lithology and deviated borehole survey logs. These logs were interpreted to yield information on the sandstone formation's subsurface structure, facies, fluid type, saturation, and temperature. Both the well logs and the production records suggest that the Nugget Sandstone is a deep saline aquifer lying at depths between 12,000 (3658 m) and 18,000 (5486 m) feet regionally, with a fluid type dominated by NaCl brine and a salinity ranging from 10,000 to 115,000 ppm. Fluid pressure data from limited logs also suggest that groundwater flow in this formation is stagnant, although near the gas plant, this information is highly uncertain due to the limited number of wells (Fig. 1).

For fluid flow simulations, well temperature data were interpolated to obtain a temperature-depth profile. At selected wells where core measurements exist, total porosity was determined from Porosity and Neutron Density logs and was calibrated against the core measurements to obtain an effective porosity. A correlation function, obtained at locations where both types of data exist, was used to calibrate well-log porosity at locations without core measurements. From the core measurements, a semi-log transform between porosity and horizontal permeability (k_H) was obtained, which is consistent with the petrophysical relations found for similar lithologies (Nelson, 1994). Nugget Sandstone permeability was observed to be isotropic in the horizontal plane, but exhibits a range of variation in the vertical direction: k_V/k_H varies from 2.0 to 0.02, although information is lacking as to whether this variability reflects in situ condition rather than an artifact of the drilling/coring process. Because the available Nugget Sandstone core specimens from the Moxa arch region do not exhibit fractures, a k_V/k_H of 1.0 is used to populate vertical permeability from the horizontal permeability. An earlier sensitivity analysis of acid gas disposal at the same study site using a smaller flow model suggests that though permeability anisotropy (i.e., smaller values of k_V/k_H) can contribute to more acid gas storage, effect of this uncertainty is relatively minor compared to that due to the uncertain relative permeability model used in the simulation study (Li et al., 2011).

2.2.2. Geostatistical reservoir modeling

Based on an interpretation of the formation top and bottom from cross sections, isopachs, and well logs, a regional structure model was built, bounded by the basin axis to the east and the Hogback Thrust Fault to the west (Fig. 1). This model is compared with the horizons interpreted from two seismic line shots in the southern Moxa arch (Stearns et al., 1975; Royse et al., 1975), showing correct formation thickness and continuity near the injection site and the neighboring region. Given the structure model, geostatistical facies modeling was conducted following three steps: (1) At each well, multiple continuous log signals (e.g., RHOB, GR, DT, NPHI) were converted to discrete petrofacies types using a hierarchical clustering algorithm (Fraley, 1998). At wells where mud logs (i.e., coded rock type) were collected, the modeled petrofacies were favorably compared to the observed lithology. (2) Experimental indicator variograms were constructed for each petrofacies in the horizontal and vertical directions. To model horizontal anisotropy, N40E was selected as the major horizontal axis, reflecting the average direction of maximum depositional continuity. (3) Based on the variogram parameters, sequential indicator simulation was used to populate facies in the model, which honors the observed petrofacies data at well locations (Ma et al., 2008, 2009). At the regional scale, a fine-grid, geostatistical petrofacies model was created with approximately 14 million grid cells.

To model $scCO_2$ injection, a section model, centered at the gas plant, was extracted from the regional model (Fig. 7). The section model size is $33{,}660 \times 114{,}066 \times 4965\ ft^3$, with 56 (E-W) × 190 (N-S) × 14 (vertical) (148,960) grid cells. Porosity and absolute permeability were then populated in the section model: (1) For each petrofacies, experimental porosity variograms were computed from the calibrated well log porosity. A spherical model was fitted from which correlation parameters were obtained. On the horizontal plane, the major and minor statistical axes of correlation were aligned with those of the facies model, thus depositional continuity is assumed to control the porosity distribution. (2) Based on the variogram parameters, porosity was populated, facies by facies, using Sequential Gaussian Simulation, a conditional geostatistical algorithm that honors the calibrated well log porosities. (3) Given the porosity model and the porosity-permeability transform relations developed for the facies, permeability was then populated (Fig. 7). A set of 200 porosity realizations was generated from which three pore volume models were selected, corresponding to 10% (P10), 50% (P50), and 90% (P90) of the total pore volume probability (note that the pore volume of the model is a stochastic quantity due to porosity variability in the inter-well region as modeled by the realizations). The P50 model is used in this study, as a prior sensitivity analysis suggests that pore volume variation among the realizations exerts a minor influence on predicting acid gas storage (Li et al., 2011).

2.3. Preliminary well selection

From visualizing the Nugget Sandstone permeability model, the top 2/3 of the formation is relatively more homogeneous while the bottom 1/3 is strongly heterogeneous with a higher variability in permeability. Because the CO_2 sweep efficiency is sensitive to the existence and degree of formation heterogeneity, preliminary simulation was carried out with this model to evaluate reservoir permeability connectivity using a single injector. In this problem, water injection was modeled using FrontSim, a streamline simulator (Schlumberger, 2009). Results suggest that lateral continuity in the bottom high-permeability facies strongly influences fluid flow,

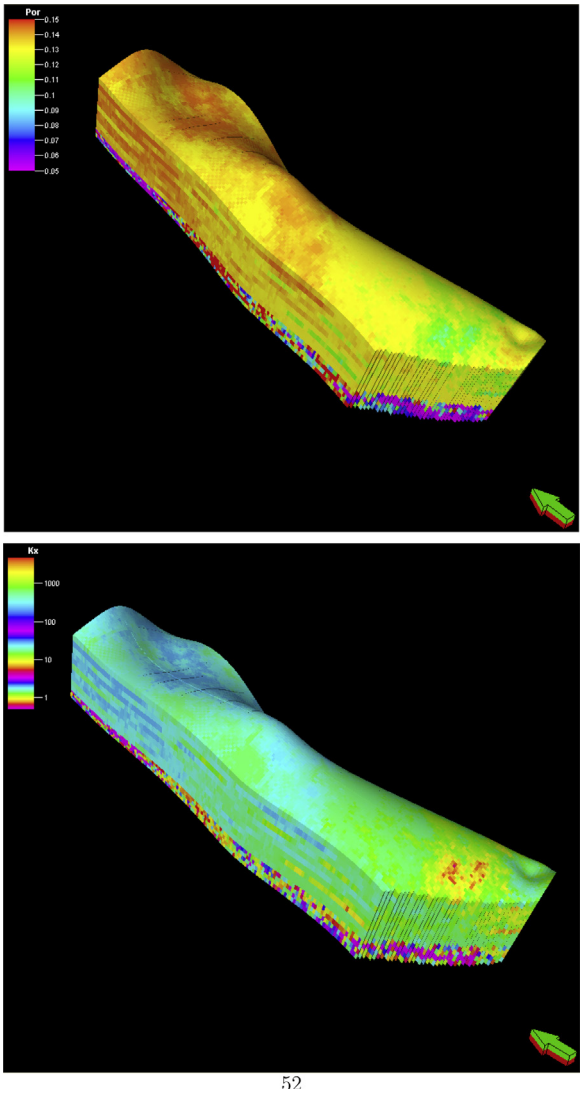

Fig. 7. (Top) Reservoir porosity and (bottom) permeability of the P50 pore volume model. Arrow points north.

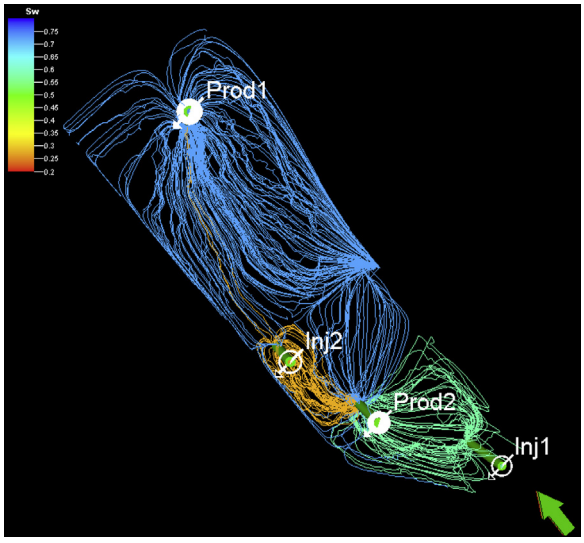

Fig. 8. Streamline simulation of a waterflood. Arrow points north.

and much of the upper formation remains unswept. To enhance sweep efficiency, more wells are needed. Because permeability connectivity significantly influences inter-well communication and reservoir sweep, location of the injection and (brine) production wells must be appropriately selected to maximize CO_2 storage. Two water injectors and two water producers, perforating the bottom half of the formation, were placed in the high permeability region of the model. The same streamline simulator was used to model the new waterflood experiment. By visualizing the streamlines, well location was adjusted until a best single-phase flow connectivity was achieved between the injectors and producers (Fig. 8).

2.4. CO_2 simulation

In this study, $scCO_2$ injection is modeled with CO2STORE of Eclipse 300, a multi-phase compositional simulator that is applicable to modeling deep saline aquifer storage (Schlumberger, 2009). Two phases are considered: a $scCO_2$ phase and a liquid or brine phase. Density of $scCO_2$ is computed using a cubic Equation of State tuned to experimental measurements. Brine density is corrected for total dissolved solids. Between the two phases, three components (CO_2, H_2O, NaCl) are modeled: CO_2 and H_2O exist in both the supercritical and the liquid phases; NaCl is always in the liquid phase. Mutual solubilities of $scCO_2$ and H_2O are calculated to match experimental data measured under typical storage conditions. When the level of total dissolved solids is high, a modified Peng-Robinson Equation of State is used to calculate $scCO_2$ solubility in the aqueous phase. CO2STORE solves the pressure and molar density of each component. The mole fractions of the components in the phases are computed through a flash process.

To initialize the model and to compute fluid properties, a single brine phase is assumed in the model, with hydrostatic pressure as the initial reservoir pressure. Reservoir temperature is populated from interpolating the temperature logs. Rock compressibility is assigned with a typical value of the Nugget Sandstone at the storage formation depth (Lachance, 1983). In the simulations, water is assumed to be the wetting phase, $scCO_2$ the non-wetting phase. To model flow reversal in a grid cell before maximum $scCO_2$ saturation is reached, the standard Carlson model is used for scanning curve interpolation (Schlumberger, 2009). This model honors the measured end-point relative permeabilities from the experiment, yielding scanning curves that are approximately parallel between the bounding $scCO_2$ drainage and imbibition curves.

To model $scCO_2$ storage, boundary conditions need to be specified for the reservoir flow model. Although both no-flow and open boundary conditions have been commonly used in modeling CO_2 storage, due to the uncertainty concerning groundwater flow in the Nugget Sandstone and the nature of reservoir compartmentalization at the Shute Creek storage site, both no-flow and flowing boundary conditions are evaluated in this study. Specifically, for streamline simulation, a no-flow boundary condition is used, while for the $scCO_2$ injection phase, a no-flow boundary condition is also used for the well optimization study (next section). At this stage, CO_2 flow is dominated by viscous force due to the pressure gradient between the injectors and producers, and boundary conditions are found to exert minor influences on storage (Li et al., 2011). For the post-$scCO_2$-injection phase (with the chase brine operation occurring in a brief initial period), both no-flow and flowing boundary conditions are evaluated due to the reduced fluid flow velocities in the reservoir. These evaluations are carried out using the optimized well design, and the simulations are run from the start of the $scCO_2$ injection using the same boundary conditions: if no-flow is assumed, it is used for the entire simulation time, and vice versa. Moreover, in the flowing boundary conditions, a background flow field is established in the reservoir, i.e., the model is open at the north and south boundaries which are connected to

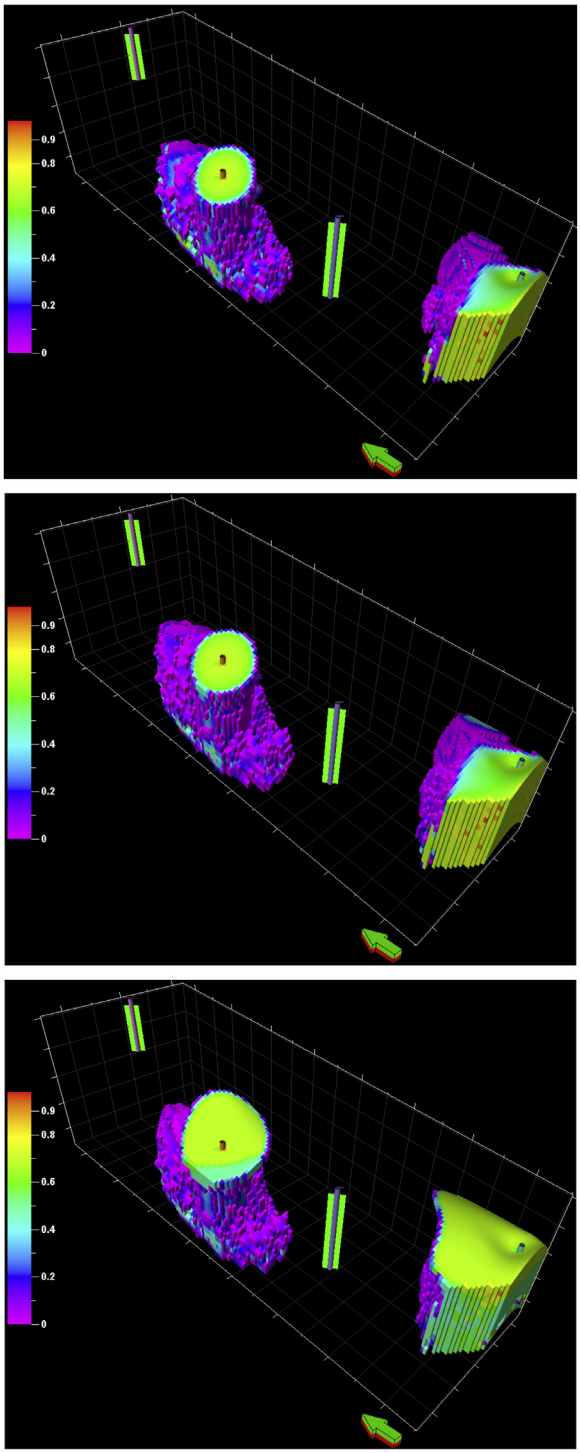

Fig. 9. Mobile $scCO_2$ saturation predicted for case B-2-2: (top) end of $scCO_2$ injection, year 50, (middle) end of chase brine injection, year 80, (bottom) end of monitoring, year 1080.

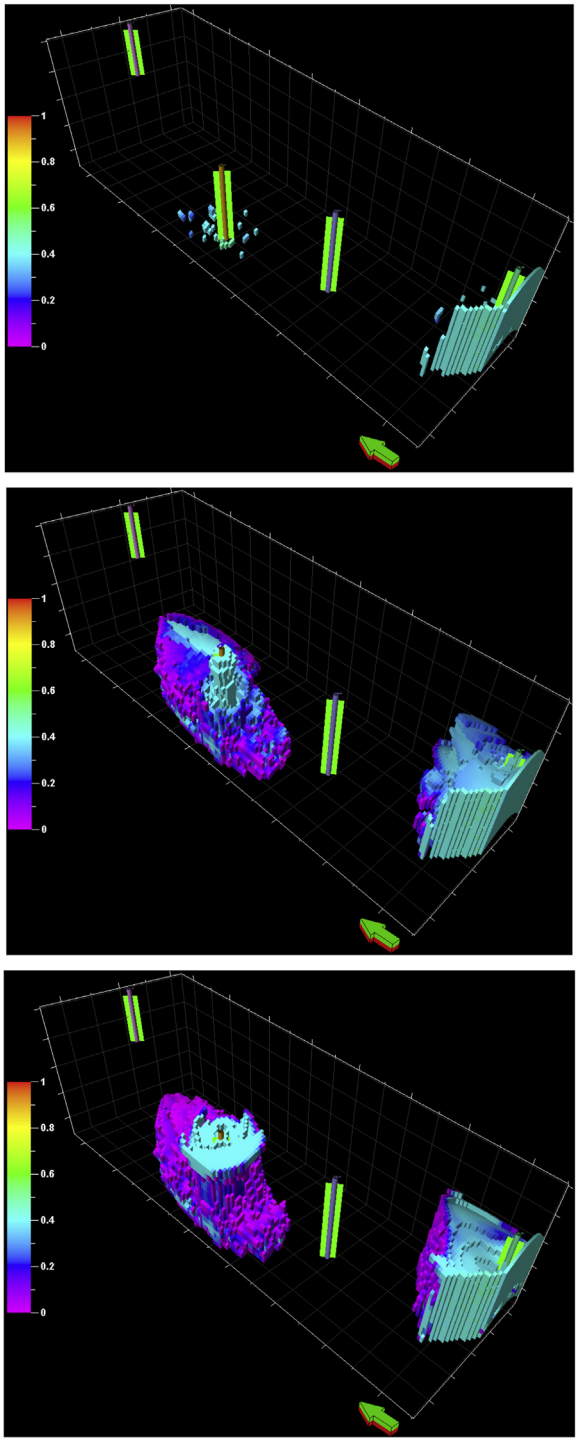

Fig. 10. Residual $scCO_2$ saturation predicted for case B-2-2: (top) end of $scCO_2$ injection, (middle) end of chase brine injection, (bottom) end of monitoring.

external aquifers with different hydraulic heads. The rest of the boundaries are sealed. A hydraulic gradient is thus established in the model, inducing groundwater flow in a north-to-south orientation at an average velocity of around 2.0 m/year. Given that the actual groundwater velocity at the storage site is unknown, this rate is selected to represent a higher end-member value that could be expected in regional aquifers in the Rocky Mountain and Great Plains regions (Godnold, 1985). This flow direction is largely parallel with the direction of $scCO_2$ migration, to be presented later.

Using well test data from the Shute Creek gas plant, a fracture gradient is determined for the reservoir at approximately 1.8 times the hydrostatic pressure gradient, which sets an injector bottomhole pressure (BHP) constraint for the simulations (Li et al., 2011). Moreover, brine producers are turned on at the same time as the $scCO_2$ injectors. Meanwhile, their BHP constraint is set lower than that of the injectors and is further adjusted for optimal CO_2 storage (see the next section). During a simulation, Eclipse 300 adjusts the injection rate down from an initial target rate, so that the maximum formation fluid pressure will not exceed the injector BHP

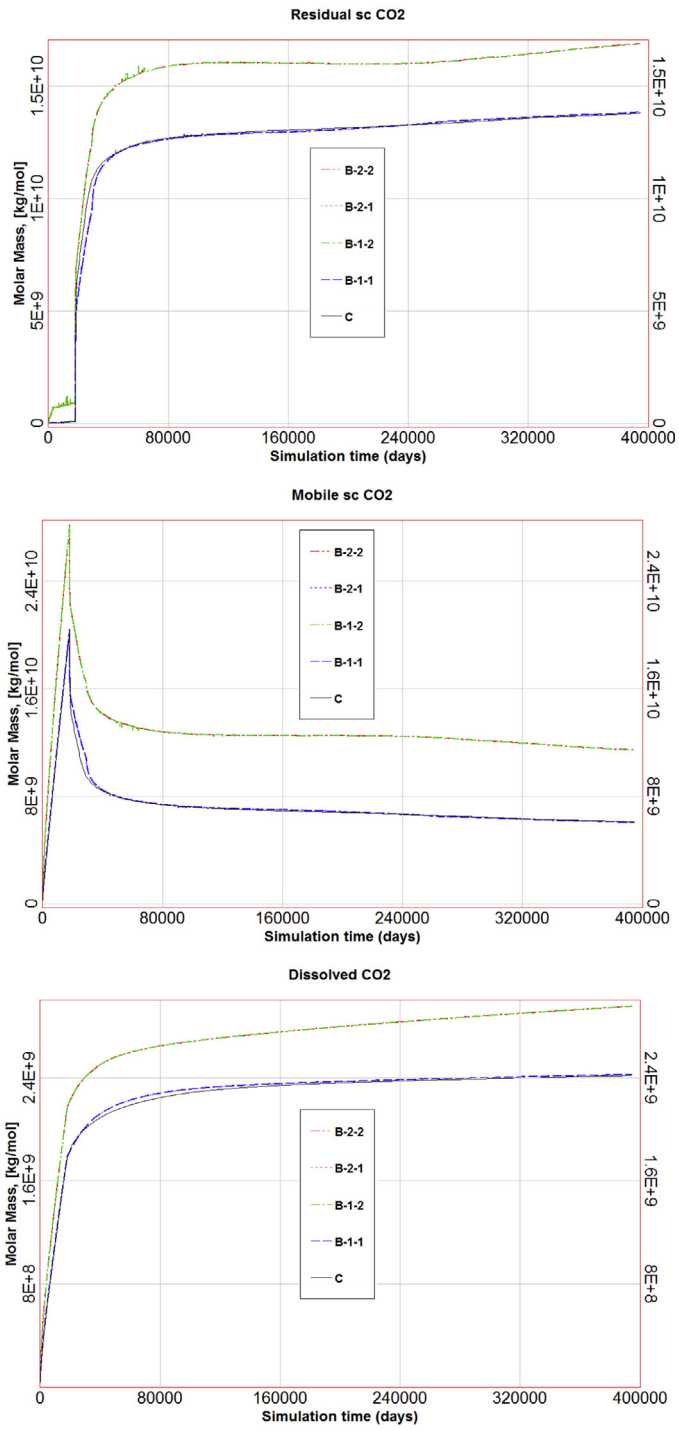

Fig. 11. (Top) Residual $scCO_2$, (middle) mobile $scCO_2$, and (bottom) dissolved CO_2 in brine predicted for all cases over the entire simulation time. (For interpretation of the references to colour in the text, the reader is referred to the web version of this article.)

constraint. The final reported injection rate by Eclipse 300 is the actual rate accomplished by the simulation while satisfying all the constraints.

2.5. Injection: maximizing CO_2-in-place

Because carbon dioxide storage involves two-phase flow and $scCO_2$ migration is subject to gravity override, well location and configuration are additionally optimized by simulating $scCO_2$ injection for 50 years, based on the initial well design obtained from analyzing single-phase connectivity (see Section 2.3). In this analysis, the initial well locations are adjusted following two design objectives: (1) $scCO_2$ plumes predicted by simulating the injection test with different well configurations are compared at the end of injection. Since a larger plume enhances $scCO_2$ trapping and dissolution, well configurations that lead to the largest plume sizes are selected, the size being defined by the number of grid cells with $scCO_2$ saturations greater than 1%. (2) For the simulation cases with the largest plume sizes, multiple BHP constraints are then selected for the brine producers. Under each constraint, the mass ratio of CO_2-in-place to the total injected CO_2, both reported by Eclipse 300, is computed at the end of injection. The best constraint is one that gives a high CO_2-in-place while maintaining a high injection rate. A lower producer BHP constraint results in a higher injection rate but at the cost of producing more CO_2; the best BHP constraint is therefore a compromise.

In the above analysis, besides varying the well locations, perforations of one or two injectors and brine producers are also varied: all wells are either fully perforated in the entire formation, perforated in the bottom one-half of the formation, or the bottom one-third. For a given set of well location and perforation intervals, simulations are also conducted testing multiple injection rates (from 40 to 80 Kt/day) and multiple producer BHP constraints (from 5275 to 6175 psi). Thus, to optimize injection-phase CO_2 storage (maximizing both the injection rate and CO_2-in-place), well locations, brine producer BHP, perforation interval(s), and the injection rate are varied. A total of 436 simulations are run for the injection phase, with results suggesting that given the same injection rate and the same BHP constraint, full or partial perforation produces similar predicted CO_2 profiles. Thus, based on the criteria of a large plume size, high CO_2-in-place, and a large CO_2 injection rate, a single "best case" design for the injection phase is selected among these simulations. It has, from north to south, an injector–producer–injector–producer (IPIP) configuration that is approximately the opposite of that shown in Fig. 8, whereas each well perforates the bottom half of the formation.

2.6. Post-injection: maximizing CO_2 trapping

With the best well design for injection-phase storage thus identified, post-injection simulation will aim to maximize $scCO_2$ trapping by introducing chase brine into the two $scCO_2$ injectors for 30 years. To maintain reservoir pressure, the same brine producers are active throughout chase brine injection. Note that the injection of "pure brine" may enhance $scCO_2$ dissolution, while the injection of CO_2 saturated brine may reduce the mobility contrast between chase brine and $scCO_2$-in-place, thus enhancing sweep efficiency. Two types of chase brine compositions are thus tested. The first type is formation brine with a total dissolved solids content of 10,000 ppm, which reflects an average Nugget Sandstone produced water salinity from three wells located closest to the gas plant. This brine is assumed not to have been in contact with $scCO_2$ and is herein referred to as "pure brine." The second type of brine is saturated with CO_2 at the formation temperature and pressure condition; this brine may reflect produced water with dissolved CO_2 at the pressure control wells. Given the chase brine choices and the need to additionally assess the potential importance of different reservoir boundary conditions (stagnant vs. open) on CO_2 storage and trapping, a set of test cases are simulated and evaluated for their storage profiles:

B-1: **Pure Chase Brine Injection**

B-1-1 No-flow is assigned as the reservoir boundary condition.

B-1-2 A background hydraulic gradient is assigned: groundwater flows from north to south.

B-2: **CO_2-Saturated Chase Brine Injection**

B-2-1 No-flow is assigned as the reservoir boundary condition.

B-2-2 A background hydraulic gradient is assigned: groundwater flows from north to south.

C: **Baseline** Passive post-$scCO_2$-injection simulation without using chase brine. No-flow is assigned as the reservoir boundary condition.

For the above cases where chase brine is employed for the first 30 years after $scCO_2$ injection has ceased, two boundary condition scenarios are modeled, representing a reservoir without or with natural background flow. In the latter scenario, background flow is assigned throughout the simulation time including the CO_2 injection phase. In simulating B-1-1, three injector perforation settings are also tested: entire formation perforated, bottom half of the formation perforated, and basal 1/3 of the formation perforated. Results suggest that full perforation traps the most residual $scCO_2$, thus a workover is simulated extending the well perforation for the monitoring phase. Next, multiple brine producer BHP constraints are tested. An optimal BHP constraint is selected which results in minimum $scCO_2$ breakthrough at the producers, while maximizing the amount of $scCO_2$ trapped in the reservoir. Therefore, in analyzing the rest of the scenarios, all chase brine injectors are perforating the full formation and a similar producer BHP is used. Compared to the chase brine cases, the Baseline case relies on natural imbibition of the migrating $scCO_2$ for residual trapping. Because no fluid injection takes place after $scCO_2$ injection ceases, all injectors and producers are shut off. Finally, for all scenarios (four chase brine cases and one Baseline), CO2STORE simulates an additional 1000 years after chase brine injection ceases. During this time, all wells are shut off and $scCO_2$ plume experiences natural imbibition as it migrates slowly towards the formation top. Additional dissolution and residual trapping then occurs. Therefore, the total simulation time includes 50 years of CO_2 injection, 30 years of chase brine injection, plus 1000 years of monitoring, for a total simulation time of 1080 years (the Baseline case simulates 50 years of injection and 1030 years of monitoring).

3. Results

3.1. CO_2 Injection simulation (best well design)

After running and analyzing a set of 436 simulations, the best case with maximum CO_2-in-place and minimum CO_2 breakthrough at the brine producers is achieved using an IPIP well configuration, injector perforation in the bottom half of the formation, and a producer BHP constraint of 6030 psi. For both boundary conditions, less than 0.1 wt% of the injected CO_2 is produced. As an example, after 50 years of injection, for the B-2-2 case, a significant amount of mobile $scCO_2$ exists in the reservoir (top panel of Fig. 9). Due to reservoir heterogeneity, two separate $scCO_2$ plumes have formed near the injectors at this time. At the reservoir top, footprints of these plumes are relatively small and are clustered around the injectors. Because $scCO_2$ is injected into the bottom half of the formation, each plume is more extensive in the lower formation, as expected. At the end of injection, the amount of residual $scCO_2$ is limited (top panel of Fig. 10). During injection, $scCO_2$ flow is dominated by the viscous drive and $scCO_2$ is continually charging the grid cells near the injectors, drainage thus dominates and the amount of the residually trapped $scCO_2$ is small. Moreover, a minor amount of residual $scCO_2$, shown in Fig. 10 (top), is probably an effect of fluid pressure fluctuation in response to plume migration through a heterogeneous reservoir and the effect of boundary conditions assigned to the model. The distribution of mobile and residual $scCO_2$ have also been examined for the other scenarios (not shown), without presenting significant differences with the simulation outcomes of the B-2-2 case.

After the best well design was identified under the no-flow boundary conditions, which leads to an injection rate of 10.77 Mt/year, the same simulation is repeated under the flowing boundary conditions, which leads to a rate of 15.13 Mt/year. These two models with alternative boundary conditions are then used for post-$scCO_2$-injection monitoring simulations. In the following, results using the flowing boundary conditions are presented, as conclusions relating to CO_2 storage profile optimization are similar.

3.2. Post-injection

With the best well design identified for the injection-phase, four chase-brine cases and one Baseline case without chase brine are simulated for the post-injection phase. In all the chase brine simulations, again, very little $scCO_2$ is produced by the end of chase brine injection. At this time, all wells are shut off, and no more brine and CO_2 are produced. For the B-2-2 case, due to the effect of gravity override, the footprint of the mobile $scCO_2$ plume has grown slightly (middle panel of Fig. 9) compared to that shown at the end of injection (top panel of Fig. 9). As for residual $scCO_2$, it grows dramatically from virtually non-existent at the end of injection to two sizable plumes surrounding the chase brine injectors (i.e., the original $scCO_2$ injectors). Significant residual trapping has occurred at this time; the residual $scCO_2$ plumes are nearly of the same sizes as the mobile $scCO_2$ plumes.

At the end of the simulation, for the B-2-2 case, the footprint of the mobile $scCO_2$ has grown larger with time (compare all panels of Fig. 9). As long as the mobile $scCO_2$ from the lower formation continues to migrate upwards and pools beneath the reservoir top, the footprint will continue to grow. As for the residual $scCO_2$ plumes, however, their dimensions changed very little compared to those observed at the end of chase brine injection. For B-2-2, soon after chase brine injection ends, the amount of residual $scCO_2$ appears to stabilize in the reservoir (top panel of Fig. 11; red curve), despite the fact that mobile $scCO_2$ is continually migrating towards the reservoir top, creating conditions for residual trapping. This is likely because the additional residually trapped $scCO_2$ is diminished by the simultaneous dissolution into the brine (bottom panel of Fig. 11; red curve).

Comparing the profiles of residual, mobile, and dissolved CO_2 over time, two distinct groupings are revealed (Fig. 11). For each CO_2 category (residual, mobile, or dissolved CO_2), predictions of the Baseline case (without chase brine, without background flow) lie close to those of B-1-1 (pure chase brine without background flow) and B-2-1 (CO_2-saturated chase brine without background flow). When the reservoir is compartmentalized, under the imposed BHP constraints, chase brine did not exert a significant influence on CO_2 predictions. In fact, the rate of chase brine injection is suppressed due to the constraint that was placed on minimizing all forms of CO_2 produced at the two brine producers. A higher rate of chase brine injection, though potentially acting to dissolve or trap more CO_2 along the flow paths, is prohibited because of the concomitant increase of CO_2 production. Thus, at the study site, under the constraints which aim to maximize CO_2-in-place, chase brine injection does not appear an effective strategy for enhancing CO_2 storage. Because of the relatively small chase brine injection rate, little difference exists between the outcomes of B-1-1 and B-2-1, thus brine chemistry does not significantly impact the CO_2 predictions. The trapping efficiency of all these cases, which is defined as the mass fraction of the residual $scCO_2$ of the total CO_2-in-place, is approximately 62% at the end of the simulation (Table 4).

Table 4
Dissolved CO_2, mobile $scCO_2$, and residual $scCO_2$ predicted for all cases. The mass unit is in 10^{10} lbm. Due to the constraints placed on CO_2 production, CO_2-in-place is approximately the same as the total injected $scCO_2$. Trapping efficiency is defined as the mass ratio of residual $scCO_2$ with respect to the total CO_2-in-place.

Cases	CO_2 categories	Simulation time (year)						
		50 (End of $scCO_2$ injection)			80 (End of chase brine injection)		1080 (End of monitoring)	
		10^{10} (lbm)	CO_2-in-place 10^{10} (lbm)	Trapping efficiency (%)	10^{10} (lbm)	Trapping efficiency (%)	10^{10} (lbm)	Trapping efficiency (%)
B-1-1	Dissolved CO_2	0.179	2.23	0.41%	0.2	42.50%	0.242	62%
	Mobile $scCO_2$	2.04			1.08		0.603	
	Residual $scCO_2$	0.0084			0.946		1.38	
B-1-2	Dissolved CO_2	0.217	3.13	3.10%	0.239	39.82%	0.295	54%
	Mobile $scCO_2$	2.82			1.65		1.14	
	Residual $scCO_2$	0.0973			1.25		1.69	
B-2-1	Dissolved CO_2	0.179	2.23	0.37%	0.2	42.70%	0.242	62%
	Mobile $scCO_2$	2.04			1.08		0.604	
	Residual $scCO_2$	0.0084			0.954		1.38	
B-2-2	Dissolved CO_2	0.179	3.13	3.11%	0.239	39.95%	0.295	54%
	Mobile $scCO_2$	2.04			1.64		1.14	
	Residual $scCO_2$	0.0084			1.25		1.69	
C	Dissolved CO_2	0.179	2.23	0.36%	0.199	48.45%	0.242	62%
	Mobile $scCO_2$	2.04			0.95		0.609	
	Residual $scCO_2$	0.00798			1.08		1.38	

The second grouping includes B-1-2 (pure chase brine with background groundwater flow) and B-2-2 (CO_2-saturated chase brine with background groundwater flow). Compared to the first group, more $scCO_2$ was injected into the reservoir, resulting in higher amounts of the predicted residual, mobile, and dissolved CO_2 (Table 4). The change in reservoir boundary conditions, from a sealed system to an open system with background flow, has resulted in a greater amount of $scCO_2$ being injected into the reservoir model. However, though their CO_2 profiles appear to be similar to those of the first group, the trapping efficiency is slightly lower at 54% at the end of the simulation.

Comparing the trapping efficiency among all cases, the Baseline (no background flow and no chase brine) has the highest trapping efficiency at the simulation time of 80 years, which corresponds to the end of chase brine application in the chase brine simulations. This suggests that natural imbibition as a result of plume migration is more effective than imbibition induced from chase brine application. This appears counterintuitive and to further understand the causes, then two additional simulations are conducted using a different set of relative permeability functions (Fig. 12), which were measured based on CO_2/brine experiments on the Viking Sandstone (Li et al., 2011). Besides the fact that the new simulations utilize the new relative permeability functions with a higher relative permeability end point compared to that of the Nugget Sandstone, the first simulation is identical to B-1-1 and the second simulation is identical to the Baseline. When comparing the results of these new simulations, an opposite effect is observed: the implementation of chase brine injection leads to a greater trapping efficiency compared to that predicted by the new Baseline case. This suggests that the efficiency of chase brine application depends on the end point of the CO_2 relative permeability function: it could be an effective approach if the Nugget Sandstone $scCO_2$ relative permeability end point is of a greater magnitude.

4. Discussion

For a proposed $scCO_2$ storage site in the Moxa arch region of Wyoming, field data and laboratory experiments, reservoir simulation, and storage optimization are integrated. Though this study evaluates $scCO_2$ storage in a single aquifer, realistic laboratory and field data, as well as site conditions, were incorporated into the simulation model, leading to a set of observations attesting to the feasibility of commercial-scale storage at the proposed site. Workflows and insights developed in this work are expected to be applicable to the design of integrated storage operations at other locations. Based on results of this study, several observations can be made:

- The $scCO_2$ end point relative permeability has a significant impact on residual trapping and the effectiveness of chase brine operation. In designing and optimizing CO_2 storage, site-specific multi-phase flow data should be collected and used in the $scCO_2$ flow model, which can lead to better engineering practices.
- In this study, the drainage and imbibition relative permeability values were obtained under capillary-dominated flow regimes. However, viscous flow could be a dominant factor near wells. This issue could be addressed by designing future experiments to study $scCO_2$ and brine relative permeabilities under viscous-dominated flows. The experimental setup is designed to handle multi-phase core-flooding experiments with temperature and pressure ranging from ambient conditions up to 140 °C and 98,626 psi (680 MPa), although in this study, the conditions selected reflect an average burial depth of the Nugget formation in the Moxa arch area of Wyoming. This reflects the goals of the scoping study which aimed to determine multiple storage sites and depths in the region in relation to the locations of the power plants. For example, a separate site lying further west, where the formation was strongly inclined, was modeled to determine if $scCO_2$ will migrate towards the outcrop area of the same formation (Zhang et al., 2015). Moreover, variability in intrinsic permeability, as observed in lower and upper Nugget Sandstone facies, may affect relative permeability and its end members. Future work will conduct detailed, facies-based analysis for the Nugget formation at different depths, allowing further refinement of the insights gained in this study.
- To manage reservoir fluid pressure, both brine producers are active during $scCO_2$ injection, and later, during chase brine injection. During $scCO_2$ injection, the produced brine needs to be disposed of; during chase brine injection, the produced brine can be recycled back into the aquifer, leading to a net zero formation "voidage rate". At the proposed storage site, the chase brine operation, whether pure formation brine or formation brine saturated

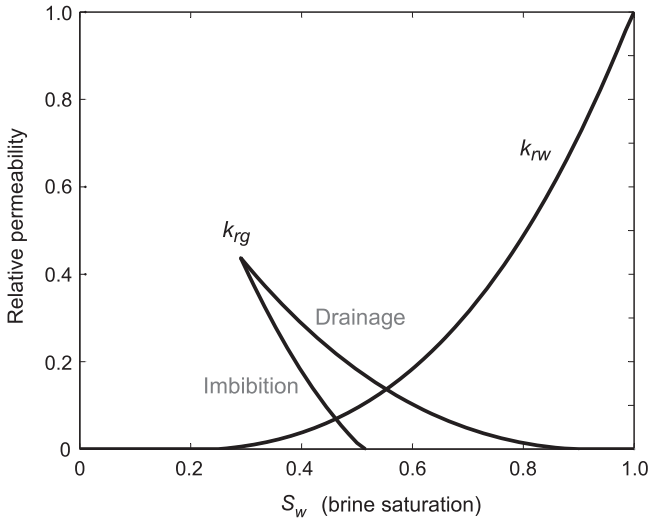

Fig. 12. Relative permeability functions for the Viking Sandstone. k_{rg} is relative permeability for the $scCO_2$ phase; k_{rw} is relative permeability for the brine phase.

with CO_2, exerts relatively little impact on the overall storage profiles. Therefore, $scCO_2$ breakthroughs at the brine producers may not be an overriding concern for the storage project if the produced brine is re-injected.

- Though longer simulation time is not modeled, using the trajectory of the trapping efficiency with time as a guide, all $scCO_2$ could be immobilized in approximately another 2000 years. This result supports the feasibility of commercial-scale geological carbon dioxide sequestration in the Nugget Sandstone in Moxa arch. Moreover, although chase brine composition did not lead to significant differences in the storage profiles, over longer time scales, residual and mobile $scCO_2$ in the reservoir will slowly dissolve into brine, thus pure brine injection should contribute to more dissolution trapping.
- Given uncertainty over the reservoir boundary conditions at the proposed storage site, an additional set of eight simulations was conducted with the best injection-phase well design, introducing background flow into the reservoir along four other directions, while the mean velocities were maintained at similar magnitudes. The Nugget Sandstone relative permeability model is used for all these simulations. These simulations, however, did not lead to significantly different storage outcomes when compared to the predictions of the previous cases with the north-to-south flow. For the given reservoir simulation condition including the constraints placed on the injectors and producers, the background flow direction, though uncertain, does not change our conclusions made about the storage profiles.

5. Conclusion

Injection of supercritical carbon dioxide ($scCO_2$) into deep saline aquifers is considered a promising option to mitigate global climate change. At a storage site, the main objectives of carbon dioxide sequestration are to maximize the volume of $scCO_2$ injected and to minimize leakage, while effectively managing formation fluid pressure buildup and brine displaced by $scCO_2$. For a proposed commercial-scale storage site in western Wyoming, this research carries out an integrated characterization-to-optimization study for carbon sequestration. Using a three-dimensional heterogeneous reservoir model of a deeply buried sandstone formation, an engineering strategy is developed to optimize storage and minimize leakage. Geological and fluid flow parameters of the model were populated using field characterization data (well logs, core measurements, cross sections, and isopachs) and state-of-the-art laboratory measurements. A multi-phase flow, high pressure-temperature core-flooding equipment, which is integrated with a medical CT-scanner set-up, was utilized to perform a series of unsteady-state drainage-imbibition experiments on a sandstone core sample. Brine and $scCO_2$ saturations were measured from the CT images, and pressure differences along the core were recorded. From these data, relative permeabilities of both fluid phases were calculated, and were subsequently used by the reservoir simulation model. While prior studies modeled carbon dioxide storage in different geological environments, this work employs site-specific fluid flow parameters for the volumetric predictions, presenting an integrated characterization-to-optimization methodology that is applicable to modeling geostorage at other locations.

By carefully designing and selecting a set of optimal well configurations that led to maximum $scCO_2$-in-place during injection and minimum $scCO_2$ breakthrough in the brine producers, an injection rate ranging from 10.8 to 15.1 Mt/year is achieved, which can accommodate CO_2 output from a medium-sized power plant for 50 years. After approximately 1000 years post-injection, up to 62% of the total injected $scCO_2$ was immobilized by residually trapping. For this sandstone reservoir, the measured $scCO_2$ relative permeability end point is low compared to some of other sandstones. As a result, post-$scCO_2$-injection chase brine operation was not found to be an effective means of enhancing residual trapping. However, additional measurements of the relative permeabilities under viscous dominant flows or for different sandstone facies (those exhibiting low to strong variability in absolute permeability) will likely lead to more refined estimates. Moreover, by modulating reservoir fluid pressure, boundary conditions exert a more significant impact on flow. Given the same well configuration and bottomhole pressure constraints, an open reservoir with a lateral background flow allows 40% more $scCO_2$ to be injected, compared to a compartmentalized system. However, background flow leads to a lower trapping efficiency – after 1000 years post injection, approximately 54% of the total injected $scCO_2$ is immobilized as residual $scCO_2$. Future research at this storage site should investigate the deep hydrodynamic condition in the saline aquifer. Research that characterizes subsurface hydraulic parameters along with fluid flow direction and boundary conditions shows promise in developing the appropriate tools and techniques for such an investigation (Irsa and Zhang, 2012; Zhang, 2014).

Acknowledgements

We acknowledge the support from the Center for Fundamental of Subsurface Flow at the School of Energy Resources of the University of Wyoming. We thank Schlumberger Information Solutions for software donation and technical support.

References

Akbarabadi, M., Piri, M., 2013. Relative permeability hysteresis and capillary trapping characteristics of supercritical CO_2/brine system: an experimental study at reservoir conditions. Adv. Water Resour. 52, 190–206.

Akbarabadi, M., Piri, M., 2015. Co-sequestration of SO_2 with supercritical CO_2 in carbonates: an experimental study of capillary trapping, relative permeability, and capillary pressure. Adv. Water Resour. 77, 44–56.

Audigane, P., Gaus, I., Czernichowski-Lauriol, I., Pruess, K., Xu, T., 2007. Two-dimensional reactive transport modeling of CO_2 injection in a saline aquifer at the Sleipner site. North Sea. Am. J. Sci. 307 (7), 974–1008, http://dx.doi.org/10.2475/07.2007.02.

Bachu, S., Bennion, B., 2009. Interfacial tension between CO_2, freshwater, and brine in the range of pressure from (2 to 27) MPa. temperature from (20 to 125) °C, and water salinity from (0 to 334000) mg L^{-1}. J. Chem. Eng. Data 54, 765–775.

Batzle, M.L., Wang, Z., 1992. Seismic properties of pore fluids. Geophysics 57 (11), 1396–1408.

Bennion, B., Bachu, S., 2005. Relative permeability characteristics for supercritical CO_2 displacing water in a variety of potential sequestration zones in Western

Canada sedimentary basin. In: SPE 95547, SPE Annual Technical Conference and Exhibition, October 9–12, Dallas, TX, http://dx.doi.org/10.2118/95547-MS.
Bennion, D.B., Bachu, S., 2006. The impact of interfacial tension and pore size distribution/capillary pressure character on CO_2 relative permeability at reservoir condition in CO_2-brine systems. In: SPE-99325, SPE/DOE Symposium on Improved Oil Recovery, 22–26 April, Tulsa, Oklahoma.
Bennion, B., Bachu, S., 2008. Drainage and imbibition relative permeability relationships for supercritical CO_2/brine and H_2S/brine systems in intergranular sandstone, carbonate, shale, and anhydrite rocks. SPE Reserv. Eval. Eng. 11 (03), 487–496.
Cox, D.L., Lindquist, S.J., Bargas, C.L., Havholm, K.G., Srivastava, R.M., 1994. Integrated modeling for optimum management of a giant gas condensate reservoir, Jurassic eolian Nugget Sandstone, Anschutz Ranch East field, Utah Overthrust (U.S.A.). CA 3: Stochastic Modeling and Geostatistics. AAPG Comput. Appl. 3.
Deng, H., Stauffer, P.H., Dai, Z., Jiao, Z., Surdam, R.C., 2012. Simulation of industrial-scale CO_2 storage: multi-scale heterogeneity and its impacts on storage capacity, injectivity and leakage. Int. J. Greenh. Gas Control 10, 397–418.
Doelger, N.M., 1987. The stratigraphy of the nugget sandstone. WGA: the thrust belt review. In: 38th Annual Field Conference Guidebook, pp. 163–178.
Fitts, J.P., Peters, C.A., 2013. Caprock fracture dissolution and CO_2 leakage. Rev. Mineral. Geochem. 77 (1), 459–479, http://dx.doi.org/10.2138/rmg.2013.77.13.
Flett, M.A., Beacher, G.J., Brantjes, J., Burt, A.J., Dauth, C., Koelmeyer, F., Lawrence, R., Leigh, S., McKenna, J., Gurton, R., Robinson, W.F., Tankersley, T., 2008. Gorgon project: subsurface evaluation of carbon dioxide disposal under Barrow Island. In: SPE-116372, SPE Asia Pacific Oil and Gas Conference and Exhibition, 20–22 October, Perth, Australia.
Fraley, C., 1998. Algorithms for model-based Gaussian hierarchical clustering. SIAM J. Sci. Comput. 20 (1), 270–281.
Garridoa, D.R., Lafortune, S., Souli, H., Dubujet, P., 2013. Impact of supercritical CO_2/water interaction on the caprock nanoporous structure. Proc. Earth Planet. Sci. 7, 738–741.
Godnold Jr., W.D., 1985. Heat flow and ground water flow in the Great Plains of the United States. J. Geodyn. 4 (1-4), 247–264.
Harstad, H., Teufel, L.W., Lorenz, J.C., Brown, S.R., 1996. Characterization and fluid flow simulation of naturally fractured Frontier Sandstone, Green River basin, Wyoming. Sandia National Lab, SAND96-1955, UC-132.
Huang, N.S., Aho, G.E., Baker, B.H., Matthews, T.R., Pottorf, R.J., 2011. Integrated reservoir modeling of a large sour-gas field with high concentrations of inerts. SPE Reserv. Eval. Eng. 14 (4), SPE-146082-PA.
IPCC, 2005. IPCC Special report on carbon dioxide capture and storage. Cambridge University Press, New York.
Irsa, J., Zhang, Y., 2012. A direct method of parameter estimation for steady state flow in heterogeneous aquifers with unknown boundary conditions. Water Resour. Res. 48 (9), W09526, http://dx.doi.org/10.1029/2011WR011756.
Juanes, R., Spiteri, E.J., Orr Jr., F.M., Blunt, M.J., 2006. Impact of relative permeability hysteresis on geological CO_2 storage. Water Resour. Res. 42 (12), http://dx.doi.org/10.1029/2005WR004806.
Kampman, N., Bickle, M., Wigley, M., Dubacq, B., 2014. Fluid flow and CO_2-fluid-mineral interactions during CO_2-storage in sedimentary basins. Chem. Geol. Rev. 369 (13), 22–50.
Kharaka, Y.K., Thordsen, J.J., Hovorka, S.D., Nance, H.S., Cole, D.R., Phelps, T.J., Knauss, K.G., 2009. Potential environmental issues of CO_2 storage in deep saline aquifers: geochemical results from the Frio-I brine pilot test, Texas, USA. Appl. Geochem. 24 (6), 1106–1112.
Lachance, D.P., 1983. Comparison of uniaxial strain and hydrostatic stress pore volume compressibilities in the Nugget Sandstone. In: SPE 11971, SPE Annual Technical Conference and Exhibition, October 5–8, 1983, San Francisco, CA.
Lamerson, P.R., 1982. The Fossil basin and its relationship to the Absaroka Thrust System, Wyoming and Utah. Geologic Studies of the Cordilleran Thrust Belt, vol. 1. Rocky Mountain Association of Geologists, pp. 279–340.
Levine, J.S., Goldberg, D.S., Lackner, K.S., Matter, J.M., Supp, M.G., Ramakrishnan, T.S., 2014. Relative permeability experiments of carbon dioxide displacing brine and their implications for carbon sequestration. Environ. Sci. Technol. 48 (1), 811–818.
Li, S., Zhang, Y., Zhang, X., 2011. Geologic modeling and fluid-flow simulation of acid gas disposal in western Wyoming. AAPG Bull. 96 (4), 635–664.
Li, S., Zhang, Y., Zhang, X., 2011. A study of conceptual model uncertainty in large-scale CO_2 storage simulation. Water Resour. Res. 47, W05534, http://dx.doi.org/10.1029/2010WR009707.
Lindquist, S.J., 1983. Nugget formation reservoir characteristics affecting production in the Overthrust Belt of southwestern Wyoming. J. Petrol. Technol. 35 (7), 1355–1365, SPE-10993-PA.
Liu, F., Lu, P., Zhu, C., Xiao, Y., 2011. Coupled reactive flow and transport modeling of CO_2 sequestration in the Mt. Simon Sandstone formation, Midwest U.S.A. Int. J. Greenh. Gas Control 5, 294–307.
Ma, Y.Z., Seto, A., Gomez, E., 2008. Frequentist meets spatialist: a marriage made in reservoir characterization and modeling. In: SPE 115836, Society of Petroleum Engineers, Denver, Colorado.
Ma, Y.Z., Seto, A., Gomez, E., 2009. Depositional facies analysis and modeling of Judy Creek reef complex of the Upper Devonian Swan Hills, Alberta, Canada. Am. Assoc. Pet. Geol. Bull. 93 (9), 1235–1256.
MacLachlan, M.E., 1972. Triassic system in geological atlas of the Rocky Mountain region. Rocky Mountain Association of Geologists, Denver, Colorado, pp. 166–176.
Martinez, M.J., Newell, P., Bishop, J.E., Tuner, D.Z., 2013. Coupled multiphase flow and geomechanics model for analysis of joint reactivation during CO_2 sequestration operations. Int. J. Greenh. Gas Control 17, 148–160, http://dx.doi.org/10.1016/j.ijggc.2013.05.008.
Mbia, E.N., Frykman, P., Nielsen, C.M., Fabricius, I.L., Pickup, G.E., Bernstone, C., 2014. Caprock compressibility and permeability and the consequences for pressure development in CO_2 storage sites. Int. J. Greenh. Gas Control 22, 139–153, http://dx.doi.org/10.1016/j.ijggc.2013.12.024.
Michael, K., Golab, A., Shulakova, V., Ennis-King, J., Allinson, G., Sharma, S., Aiken, T., 2010. Geological storage of CO_2 in saline aquifers – a review of the experience from existing storage operations. Int. J. Greenh. Gas Control 4 (4), 659–667.
Nelson, P.H., 1994. Permeability-porosity relationships in sedimentary rocks. Log Anal. 35 (3), 38–62.
Olabode, A., Radonjic, M., 2013. Experimental investigations of caprock integrity in CO_2 sequestration. Energy Proc. 37, 5014–5025.
Peterson, J.A., 1972. Triassic system in geological atlas of the Rocky Mountain region. Rocky Mountain Association of Geologists, Denver, Colorado, pp. 177–189.
Picard, M.D.,1975. Facies, petrography and petroleum potential of Nugget Sandstone (Jurassic) southwestern Wyoming and northeastern Utah. In: Symposium on Deep Drilling Frontiers in the central Rocky Mountains. Rocky Mountain Association of Geologists, pp. 109–128.
Pini, R., Benson, S.M., 2013. Simultaneous determination of capillary pressure and relative permeability curves from core-flooding experiments with various fluid pairs. Water Resour. Res. 49 (6), 3516–3530.
Piri, M., 2012. Recirculating, constant backpressure core flooding apparatus and method. US2012/0211089 A1.
Qi, R., LaForce, T.C., Blunt, M.J., 2009. Design of carbon dioxide storage in aquifers. Int. J. Greenh. Gas Control 3 (2), 195–205.
Rosenbauer, R.J., Koksalan, T., Palandri, J.L., 2005. Experimental investigation of CO_2-brine-rock interactions at elevated temperature and pressure: implications for CO_2 sequestration in deep-saline aquifers. Fuel Process. Technol. 86 (14-15), 1581–1597.
Royse, F., Warner, M.A., Reese, D.L., 1975. Thrust Belt structural geometry and related stratigraphic problems, Wyoming-Idaho-northern Utah. In: Symposium on Deep Drilling Frontiers in the Central Rocky Mountains, Rocky Mountain Association of Geologists, pp. 41–54.
Royse Jr., F., 1982. An overview of the geological structure of the Thrust Belt in Wyoming, northern Utah and eastern Idaho. Geological Survey of Wyoming Memoir No. 5., pp. 273–311.
Sahni, A., Burger, J., Blunt, M., 1998. Measurement of three phase relative permeability during gravity drainage using CT. In: SPE-39655, SPE/DOE Improved Oil Recovery Symposium, 19–22 April, Tulsa, Oklahoma.
Schlumberger, Inc., 2009. Eclipse Technical Description, 2009.1.
Shukla, R., Ranjith, P., Haque, A., Choi, X., 2010. A review of studies on CO_2 sequestration and caprock integrity. Fuel 89 (10), 2651–2664.
Smith, J., Durucan, S., Korre, A., Shi, J.Q., 2011. Carbon dioxide storage risk assessment: analysis of caprock fracture network connectivity. Int. J. Greenh. Gas Control 5 (2), 226–240, http://dx.doi.org/10.1016/j.ijggc.2010.10.002.
Song, J., Zhang, D., 2013. Comprehensive review of caprock-sealing mechanisms for geologic carbon sequestration. Environ. Sci. Technol. 47 (1), 9–22, http://dx.doi.org/10.1021/es301610p.
Span, R., Wagner, W., 1995. A new equation of state for carbon dioxide covering the fluid region from the triple-point temperature to 1100 K at pressure up to 800 MPa. J. Phys. Chem. Ref. Data 25 (6), 1509–1596.
Stauffer, P.H., Surdam, R.C., Jiao, Z., Miller, T.A., Bentley, R.D., 2009. Combining geological data and numerical modeling to improve estimates of the CO_2 sequestration potential of the rock springs uplift, Wyoming. Energy Proc. 1, 2717–2724.
Stearns, D.W., Sacrison, W.R., Hanson, R.C.,1975. Structural history of southwestern Wyoming as evidenced from outcrop and seismic. In: Symposium on Deep Drilling Frontiers in the Central Rocky Mountains. Rocky Mountain Association of Geologists, pp. 9–20.
Surdam, R., Jiao, Z., Stauffer, P., Miller, T., 2009. An integrated strategy for carbon management combining geological CO_2 sequestration, displaced fluid production, and water treatment. Wyoming State Geological Survey Challenges in Geologic Resource Development, No. 8.
U.S. Energy Information Administration, 2014. State-level energy-related carbon dioxide emissions, 2000–2011.
Vilarrasa, V., Olivella, S., Carrera, J., Rutqvist, J., 2014. Long term impacts of cold CO_2 injection on the caprock integrity. Int. J. Greenh. Gas Control 24, 1–13.
WIA, 2013. Wyoming infrastructure authority (WIA) summary of activities – Report to stakeholders dated June 6.
Zhang, Y., Yang, G., Li, S., 2015. Significance of conceptual model uncertainty in simulating carbon sequestration a deep inclined saline aquifer. J. Hazard. Toxic Radioact. Waste 19 (3), 04014036, http://dx.doi.org/10.1061/(ASCE)HZ.2153-5515.0000246.
Zhang, Y., 2014. Nonlinear inversion of an unconfined aquifer: simultaneous estimation of heterogeneous hydraulic conductivities, recharge rates, and boundary conditions. Transp. Porous Media 102 (2), 275–299, http://dx.doi.org/10.1007/s11242-014-0275-x.